

# Year-Long Vertical Velocity Statistics Derived from Doppler Lidar Data for the Continental Convective Boundary Layer

LARRY K. BERG AND ROB K. NEWSOM

*Pacific Northwest National Laboratory, Richland, Washington*

DAVID D. TURNER

*Global Systems Division, NOAA/Earth System Research Laboratory, Boulder, Colorado*

(Manuscript received 7 November 2016, in final form 23 May 2017)

## ABSTRACT

One year of coherent Doppler lidar data collected at the U.S. Department of Energy's Atmospheric Radiation Measurement site in Oklahoma was analyzed to provide profiles of vertical velocity variance, skewness, and kurtosis for cases of cloud-free convective boundary layers. The variance was normalized by the Deardorff convective velocity scale, which was successful when the boundary layer depth was stationary but failed in situations in which the layer was changing rapidly. In this study, the data are sorted according to time of day, season, wind direction, surface shear stress, degree of instability, and wind shear across the boundary layer top. The normalized variance was found to have its peak value near a normalized height of 0.25. The magnitude of the variance changes with season, shear stress, degree of instability, and wind shear across the boundary layer top. The skewness was largest in the top half of the boundary layer (with the exception of wintertime conditions). The skewness was also found to be a function of the season, shear stress, and wind shear across the boundary layer top. Like skewness, the vertical profile of kurtosis followed a consistent pattern, with peak values near the boundary layer top. The normalized altitude of the peak values of kurtosis was found to be higher when there was a large amount of wind shear at the boundary layer top.

## 1. Introduction and motivation

Vertical velocity  $w$  plays a critical role in many atmospheric processes. Within the daytime continental convective boundary layer (CBL) over flat terrain, variations in  $w$  are generally associated with thermals generated by surface heating, turbulence induced by wind shear, or a combination of both processes. The thermals lead to rapid mixing of heat, moisture, momentum, and trace gases over the depth of the layer, and the role of individual thermals has been well documented (e.g., [Lenschow and Stephens 1980](#); [Greenhut and Khalsa 1987](#); [Williams and Hacker 1992](#)). If a thermal rises high enough that it reaches its lifting condensation level, then the water vapor in the thermal will condense and a cloud-topped boundary layer will form. A wide range of studies have focused on the analysis of the cloud-topped boundary in both continental (e.g., [Berg and Kassianov 2008](#); [Berg et al. 2011](#); [Fang et al.](#)

[2014](#)) and maritime (e.g., [Bretherton and Wyant 1997](#); [Ghate et al. 2014](#)) conditions.

Distributions of  $w$  are a key part of many cumulus parameterizations used in regional and global models. For example, some approaches explicitly use joint distributions of temperature and  $w$  ([Larson et al. 2012](#)), and others use the variance of  $w$  ([Bretherton et al. 2004](#)). Other parameterizations use closure assumptions related to the cumulus mass flux, which is tightly coupled to the speed of the convective updrafts for deep convection ([Kain and Fritsch 1990](#)) as well as for mixtures of deep and shallow convection ([Kain 2004](#); [Berg and Stull 2005](#); [Berg et al. 2013](#)).

There are relatively few long-term measurements of  $w$  statistics within the CBL. Most studies have focused on the analysis of a relatively small number of measurements from aircraft (e.g., [Lenschow et al. 1980](#); [Lenschow and Sun 2007](#)) or remotely piloted aircraft ([Martin et al. 2014](#)). These studies are episodic, and, while the measurements are highly useful, it is difficult to know how representative they are. Even studies with routine aircraft observations ([Vogelmann et al. 2012](#))

---

*Corresponding author:* Larry K. Berg, [larry.berg@pnnl.gov](mailto:larry.berg@pnnl.gov)

still only have a relatively small number of flights. Other studies have utilized tower data to examine  $w$  statistics (e.g., Wyngaard et al. 1971; Wood et al. 2010; Liu et al. 2011). The short height of the towers (relative to the depth of the daytime boundary layer), however, has caused some researchers to focus on the analysis of shallow internal boundary layers (e.g., Smedman and Högström 1983). Other approaches that have been applied include tank studies (Deardorff and Willis 1985) or large-eddy simulation (e.g., Deardorff 1974; Lenschow et al. 2012; Darbieu et al. 2015) to document changes in the  $w$  statistics with altitude. Coherent Doppler lidar (CDL) data have been used more recently to document not only the  $w$  variance  $\sigma_w^2$  but also higher-order moments of the distribution such as the skewness and kurtosis (Hogan et al. 2009; Lenschow et al. 2012; Röhner and Trümmer 2013; Maurer et al. 2016; Davis et al. 2013).

The long-term deployment of CDLs by the U.S. Department of Energy's Atmospheric Radiation Measurement (ARM) Climate Research Facility (Mather and Voyles 2012) gives a unique opportunity to address these shortcomings and to provide a long-term dataset that can be analyzed to document the behavior of  $\sigma_w^2$ , skewness, and kurtosis over a multiseason period at a single site. Long-term measurements of the turbulent structure of the CBL have been obtained by other ARM systems; for example, Turner et al. (2014) have used high-resolution Raman lidar data to look at water vapor variance and skewness in the CBL. Other studies have linked the properties of the shallow cumuli with the surface fluxes (Berg and Kassianov 2008; Zhang and Klein 2010), but no studies have utilized long-term data from the CDL deployed at the site. In this study, 1 yr of CBL data is used to investigate the behavior of  $w$  statistics over the full seasonal cycle.

This paper is organized in the following way: Details of the instrument systems used in the study, including the CDL as well as other instruments, are described in section 2. Section 3 presents analyses and results that are focused on changes in  $w$  statistics as a function of time of day as well as a range of other variables, such as season, wind direction, static stability, friction velocity (surface shear stress), and wind shear across the boundary layer top. Overall, systematic differences in the variance, skewness, and kurtosis are found that are related to changes in these variables.

## 2. Instruments

### a. Coherent Doppler lidar

A detailed description of the configuration and operation of the Halo Photonics CDL deployed at the

ARM Southern Great Plains (SGP; Sisterson et al. 2016) Central Facility site is presented by Pearson et al. (2009) and Newsom (2012). In brief, the system uses a near-IR laser (wavelength of  $1.5\ \mu\text{m}$ ) that is sensitive to the backscatter from aerosol and clouds to provide measurements of radial velocity and attenuated backscatter. As configured at the SGP, the CDL has a height resolution of 30 m but can be set to have a resolution between 18 and 60 m. It is important to note that the maximum range of the CDL is limited by the presence of aerosol, which generally limits retrievals of  $w$  statistics to the heights within the boundary layer, which has implications in the analysis of the data presented in this study. The CDL is configured to stare vertically for the majority of the time. Once every 15 min, the unit performs plan position indicator scans that are used to compute the mean wind profile on the basis of the traditional velocity–azimuth display algorithm (Browning and Wexler 1968; Banta et al. 2002).

The time series of  $w$  from the CDL clearly shows the presence of convective updrafts and downdrafts during convective periods (Fig. 1). These data can be combined directly to form probability density functions (PDFs) of uncorrected  $w$  ( $w$  values that include instrument noise). An ARM value-added product has been developed that takes the 1-Hz data (as shown in Fig. 1) and computes values of the higher-order moments of the  $w$  distribution (variance, skewness, and kurtosis) derived from the CDL data with a time resolution of 30 min (Newsom et al. 2015). Each 10-min value is not independent, however, because it is computed using a moving 30-min average. Thus, we only use every third value reported in our analysis. One key step in the processing of CDL data is the removal of instrument noise from the lidar's variance estimates. In our processing, the instrument noise is estimated using the method that is described by Lenschow et al. (2000) and Pearson et al. (2009). In this approach, the noise contribution to the raw radial velocity variance is determined from a time series analysis of the radial velocity data. Once the instrument noise is determined, it is subtracted from the raw variance, leaving only the atmospheric contribution. Calculation of the third- and fourth-order moments is handled differently. These quantities are computed directly by first removing radial velocities corresponding to wideband signal-to-noise ratios ( $w\text{SNR}$ ; Iwai et al. 2013) below 0.008.

Even with the noise compensation, it is well known that CDL  $w$  variance measurements are biased toward lower values because of the spatial-averaging effect caused by the laser pulse width and the range-gate size. Preliminary analysis of field data collected during a recent field campaign at the Boulder Atmospheric Observatory (Lundquist et al. 2017) suggests that the ARM

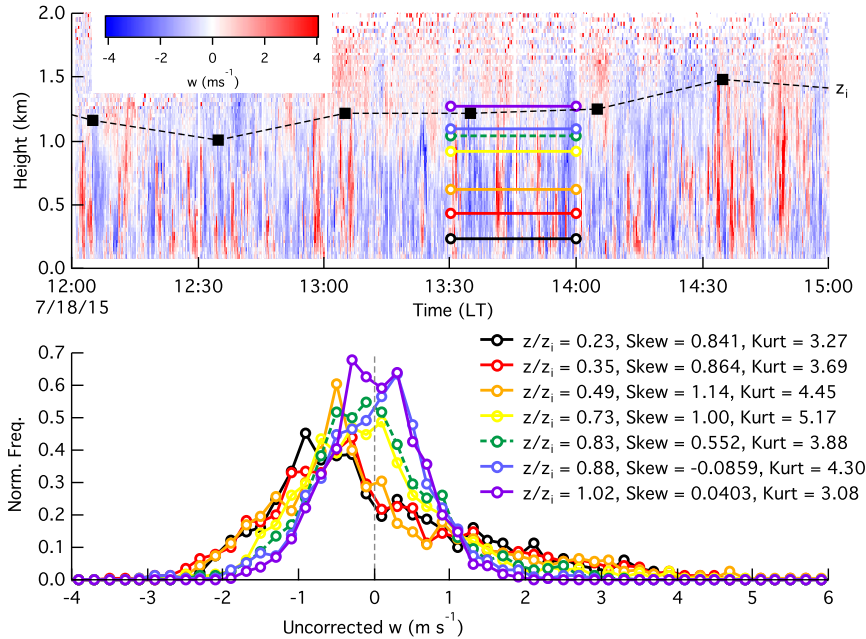


FIG. 1. Time–height cross section of uncorrected  $w$  (shading),  $z_i$  (black line), and intervals and heights used for computing sample PDFs (colors) and PDFs of  $w$  for the respective time and heights on 18 Jul 2015.

CDL  $w$  variance estimates are negatively biased by approximately 9% when the range-gate size is 30 m (Newsom et al. 2017).

Long-term averages of  $\sigma_w^2$  profiles developed from vertically staring data acquired by the CDL at the SGP Central Facility using data collected between 2010 and 2014 show a nonphysical height-dependent sinusoidal modulation of the atmospheric variance profile. The artifact is most evident in mean variance profiles during hot summer afternoon periods when the internal temperature of the CDL approaches or exceeds 40°C. In July of 2014, the CDL experienced a failure of its main control computer and was subsequently shipped back to the vendor for repair and refurbishment. The refurbishment included the installation of a new control computer and a receiver upgrade. After this work was complete, the system was reinstalled at SGP and brought back into operation in November of 2014. Subsequent analysis of data acquired after this date showed no sign of the oscillatory artifact. Although the exact cause of the artifact has not been firmly established, indications are that it was temperature related. In this study, we use only data collected during 2015, after the refurbishment of the CDL.

The CDL can also be used to measure the cloud-base height and to estimate cloud fraction, because it is very sensitive to the backscatter from cloud drops and ice crystals. The ARM CDLs estimate cloud-base heights

from the wSNR data using a matched-filter approach (Newsom et al. 2015). The ARM SGP site has a number of other instruments from which data are combined to provide detailed information about the clouds above the site; these instruments include cloud radars and laser ceilometers (Clothiaux et al. 2000) that have been used in previous studies (e.g., Dong et al. 2005; Berg and Kassianov 2008). In this study, the cloud-base-height estimates are used to mask out regions affected by clouds, because we are most interested in the identification of periods that are cloud free rather than in the details of the cloud field that can be determined from the other systems deployed at the site.

One key component of our analysis is the scaling of height by the boundary layer depth  $z_i$ . In the case of CDL systems, the  $w$  variance can be used to estimate the value of  $z_i$  by applying a threshold value. In our study, we experimented with the threshold value of  $0.04 \text{ m}^2 \text{ s}^{-2}$ , as suggested by Tucker et al. (2009). This method has the advantage that it applies a direct measure of the turbulence intensity and is less susceptible to the presence of residual layers that can fool lidar retrievals of  $z_i$  that are based on only the aerosol backscatter. At the SGP site, however, this threshold often resulted in an estimate of  $z_i$  that was too large because of gravity waves or other weak coherent vertical motions above the convective boundary layer. Definition of a single threshold is also difficult when the turbulence intensity can vary greatly

during the day or over different seasons. With these considerations in mind, the boundary layer depth is defined in this study by using a threshold of normalized variance ( $\sigma_w^2/w_*^2$ ), where  $w_*$  is the Deardorff convective velocity scale  $\{=[gz_i(w'\theta')/\bar{\theta}]^{1/3}\}$ ; the overbar indicates a time average, and the primes indicate perturbations from the mean quantity. In this case, impacts of moisture on the buoyancy have been ignored. A threshold value of 0.072 for  $\sigma_w^2/w_*^2$  is used to be consistent with the curve presented by [Lenschow et al. \(2012\)](#). An iterative approach is needed because  $w_*$  is also a function of  $z_i$ , and the initial guess of  $z_i$  is determined by using the variance threshold applied by [Tucker et al. \(2009\)](#). We found the approach to be very stable if the variance profile decreases monotonically with height. This is generally the case, but there are instances in which there is a local maximum in variance aloft and the iterative procedure jumps between two specific heights. In such cases, we simply use the smaller value of  $z_i$  as the true CBL depth. A number of techniques were considered in the context of this study, including methods reviewed by [Seibert et al. \(2000\)](#). These techniques consist of those based on the temperature lapse rate (e.g., [Heffter 1980](#); [Liu and Liang 2010](#)), temperature excess of near-surface parcels (e.g., [Holzworth 1964, 1967](#)), or the bulk Richardson number ([Troen and Mahrt 1986](#)). Other methods using remote sensing data have also been utilized in the past, including sodars and radar wind profilers (e.g., [Beyrich 1997](#); [White et al. 1999](#); [Bianco and Wilczak 2002](#)), water vapor variance profiles ([Turner et al. 2014](#)), and aerosol backscatter from surface or airborne lidars ([Brooks 2003](#); [Scarino et al. 2014](#)).

### b. Radar wind profiler

Data from the 915-MHz radar wind profiler (RWP; [Muradyan et al. 1998](#)) operated at the SGP are, in many ways, complementary to the data collected by the CDL, albeit with a much higher first range gate and coarser height and time resolution. The RWP, however, has a greater vertical range and provides measurements to heights well above  $z_i$  on many occasions. For this reason, RWP data are used to compute the wind shear across the boundary layer top using differences in the wind speed measured at  $1.1z_i$  and  $0.9z_i$ . This choice of heights is somewhat arbitrary, but the goal of this specific analysis is to break the data into cases with relatively large and small amounts of wind shear across the boundary layer top, which should not be overly sensitive to the exact heights that are selected. Data from the RWP are collected using high and low power settings to form hourly consensus averages. In this analysis, only data from the lower power setting are used because they have finer spatial resolution. Additional details of the

operation of the RWP at the ARM sites are presented by [Coulter \(2012\)](#).

### c. Surface measurements

Data from the eddy-covariance (ECOR; [Cook 1997](#)) system deployed at the ARM SGP are used to compute the sensible heat flux and typical scaling velocities, including  $w_*$  and the friction velocity  $u_* = \{[(\overline{u'w'})^2 + (\overline{v'w'})^2]^{1/4}\}$ , where  $u$  and  $v$  are the horizontal wind components. The ARM ECOR system consists of a Gill Instruments, Ltd., WindMaster Pro mounted at the top of a 10-m-tall tower along the northern edge of a field adjacent to the SGP. Thus, the best fetch for surface flux measurements are for conditions with southerly winds. Half-hour averages of the surface sensible and latent heat flux, momentum flux, and  $u_*$  are computed.

The calculation of  $w_*$  also requires mean potential temperature. The ECOR system reports temperature as measured by the sonic anemometer, but it can be biased ([Cook 2016](#)). Therefore, in our calculation, we utilize the mean temperature measured by the weather station ([Holdridge and Kyrouac 1993](#)) deployed near the ECOR system rather than the mean temperature derived from the sonic anemometer.

## 3. Selection criteria

A number of different criteria are used to select specific time periods used in the analysis, including thresholds related to the cloud fraction and the wSNR. Given that this study is focused on cloud-free conditions, we required that the cloud fraction computed from the CDL be less than 0.001 (derived from the fraction of time over a 0.5-h interval in which a cloud was detected by the CDL at any height between 100 and 9600 m). Note that using this definition leads to the inclusion of clear periods in an otherwise cloudy day. This treatment maximizes the number of points used in the analysis. Future studies may wish to apply more stringent criteria. A wSNR threshold was applied to ensure sufficient signal strength. Different wSNR thresholds were applied for the variance (0.007) and skewness and kurtosis (0.02). These different thresholds were used because the higher-order moments are inherently noisier and benefit from a higher value of wSNR while using a smaller threshold for the variance allows us to include more data points in the analysis. Using a larger wSNR threshold has the side effect of reducing the number of observations of skewness and kurtosis and leads to some differences in the number of observations within specific height ranges. Two other preliminary selection criteria are also applied to the CDL time series, including requiring that the value of sensible heat flux be positive

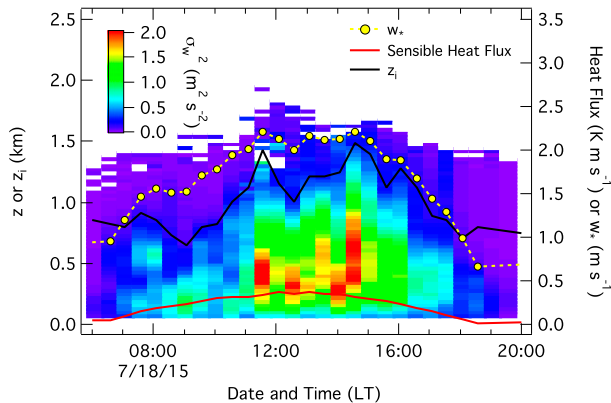


FIG. 2. Time–height cross section of  $\sigma_w^2/w_*^2$  (colors),  $w_*$  (yellow circles), surface sensible heat flux (red line), and  $z_i$  (black line) on 18 Jul 2015.

and that the value of  $z_i$  be greater than 0.2 km. These two criteria are applied to ensure that the boundary layer was truly convective. A number of different selection criteria that are focused on specific processes within the CBL, such as the season, time of day, stability, shear stress, and wind shear across the boundary layer top, are also applied, forming the basis of the analysis that is presented in the next section. In total, several thousand individual 1-h periods were selected for analysis.

**4. Analysis and results**

Over the course of any given day, the cycles of  $\sigma_w^2$ , sensible heat flux,  $w_*$ , and  $z_i$  follow a well-established pattern that is tightly coupled to the solar heating of the surface. The value of  $\sigma_w^2$  shows much variability and does not simply increase in magnitude as the day progresses. For example,  $\sigma_w^2$ , surface sensible heat flux,  $w_*$ , and  $z_i$  are plotted in Fig. 2 for 18 July 2015. As expected,  $\sigma_w^2$  is small early in the morning and has peak values that are as large as  $2.0 \text{ m}^2 \text{ s}^{-2}$  between 1700 and 2100 LT. The value of  $z_i$  also follows the expected pattern, reaching its peak value between 1100 and 1200 LT and then slowly decreasing through the rest of the afternoon. The value of  $\sigma_w^2$  was relatively large on this day ( $>2.0 \text{ m}^2 \text{ s}^{-2}$  for much of the afternoon). The growth in  $\sigma_w^2$  is not constant, however, and one of the most striking features shown in Fig. 2 is the pulses seen in the vertical velocity variance over individual 0.5-h periods. This is likely due to the relatively small number of thermals that pass over the lidar over each sampling period. For this case, the convective time scale ( $t_* = z_i/w$ ) ranges between 10 and 15 min, which is a large fraction of the sampling period.

Composites of  $\sigma_w^2$ , skewness, and kurtosis have been constructed using all of the CDL data collected during 2015 that met the criteria presented in section 3 (Fig. 3).

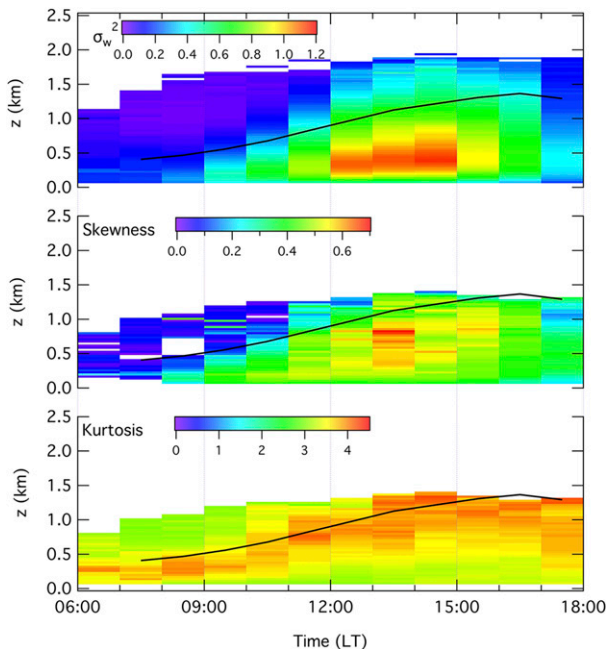


FIG. 3. Composite time series of (top)  $\sigma_w^2/w_*^2$ , (middle) skewness, and (bottom) kurtosis using all available data collected in 2015 that meet the criteria described in the text. The black solid lines represent the median values of  $z_i$ .

The  $\sigma_w^2$  follows the same pattern as the example shown in Fig. 2, and the peak values are found between 1200 and 1500 LT. The value of  $z_i$  increases rapidly between 0900 and 1200 LT and is then generally constant until 1700 LT, at which point it decreases quickly. Within the planetary boundary layer, the  $w$  skewness is positive, reaching values nearly as large as 0.7. This result is consistent with the findings of others for the daytime CBL (Lenschow et al. 2012). During the morning hours, the skewness above the boundary layer is much closer to zero. Note that the vertical extent of the skewness (and kurtosis) composites do not reach as high an altitude as the  $\sigma_w^2$ ; this difference is due to the application of different wSNR thresholds, as discussed in section 3. The kurtosis pattern is slightly different, with peak values of kurtosis found near the boundary layer top, with values in the lower part of the boundary layer being near 3 and values at the boundary layer top being 4 or slightly greater. These values indicate that  $w$  distributions found near the boundary layer top have a greater frequency of outliers than at lower altitudes, although the distribution itself tends to be narrower, as indicated by the smaller values of variance at those heights.

Although the composites, such as those shown in Fig. 3, provide information about the variation of the  $w$  statistics, additional insight can be gained by carefully investigating their sensitivity to a number of different

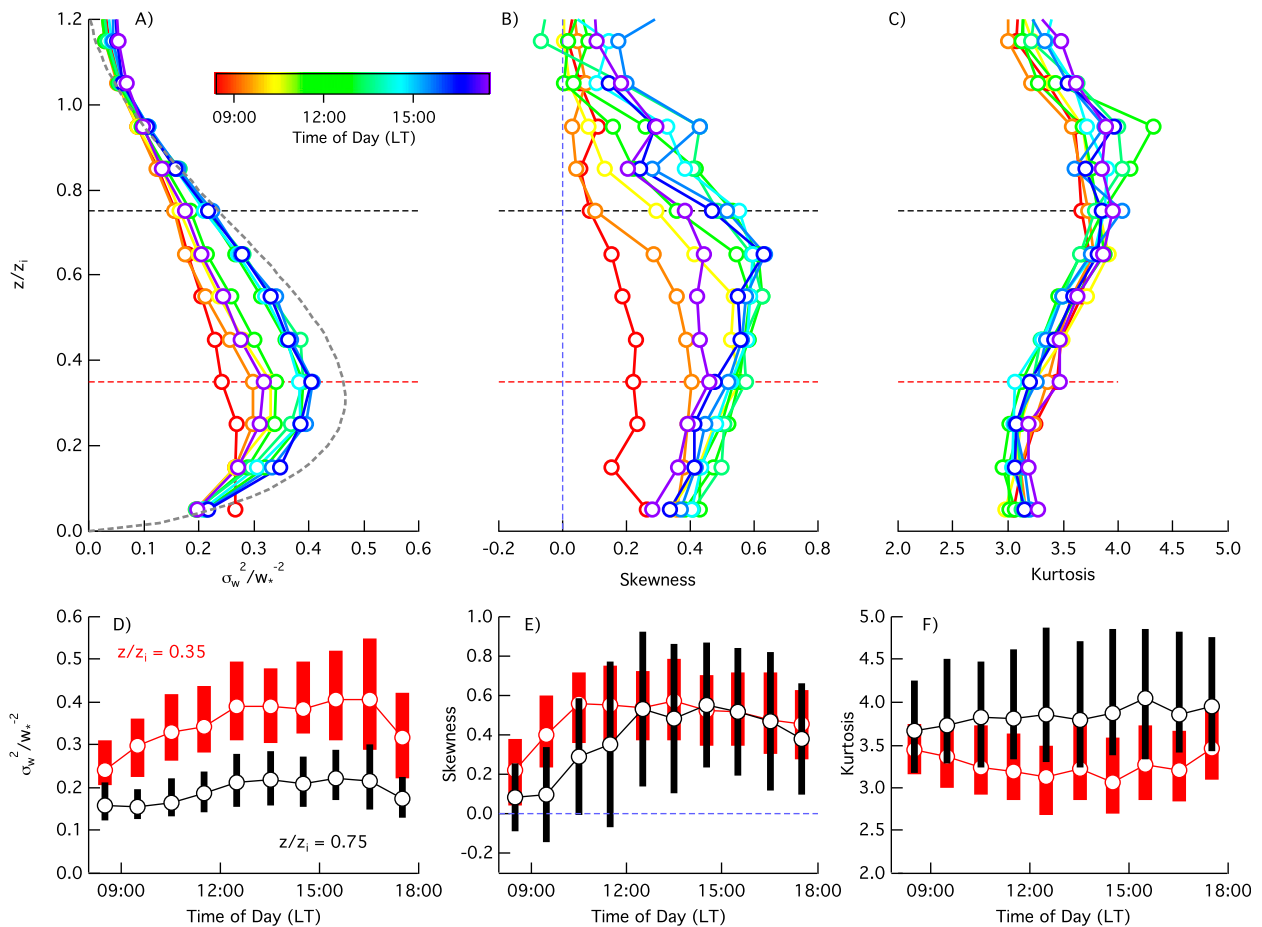


FIG. 4. Profiles of median (a)  $\sigma_w^2/w_*^2$ , (b) skewness, and (c) kurtosis as a function of time of day (colors) during 2015, and time series of (d)  $\sigma_w^2/w_*^2$ , (e) skewness, and (f) kurtosis at altitudes of  $0.35z_i$  (red) and  $0.75z_i$  (black). The open circles in (d)–(f) represent the median values, and bars indicate the 75th and 25th percentiles. The dashed line in (a) indicates the fit that was proposed by [Lenschow et al. \(2012\)](#).

factors, including the time of day, the wind direction, the season,  $u_*$ , static stability, and wind shear at the top of the boundary layer. These sensitivity studies are presented in the next sections.

#### a. Variation with time of day

The intensity of turbulence within the boundary layer clearly changes with time during the day, but scaling parameters such as  $w_*$ , combinations of  $w_*$  and  $u_*$  ([Moeng and Sullivan 1994](#)), and  $z_i$  are frequently used to make profiles of normalized key variables that are invariant with time (e.g., [Stull 1988](#); [Moeng and Sullivan 1994](#)). Analysis of the CDL data allows us to investigate the performance of the scaling more carefully. Profiles of the median  $\sigma_w^2/w_*^2$  show that the shape of the profile does not change significantly over the course of the day (with a peak value near an altitude of  $0.25z_i$ ), which is consistent with the sample PDFs highlighted in [Fig. 1](#).

The magnitude of the normalized variance increases from 0830 to 1230 LT ([Fig. 4a](#)) but is then nearly constant from 1230 to 1600 LT, after which it decreases. Similar results are found regardless of the altitude, although the response is more muted higher in the boundary layer ([Fig. 4d](#)). This breakdown in the standard scaling is likely associated with the relatively rapid growth of the boundary layer through the morning. As shown in [Fig. 3](#), the boundary layer grows rapidly between 0800 and 1200 LT. During this transitional period, the scaling using  $w_*$  and  $z_i$  breaks down, leading to profiles of  $\sigma_w^2/w_*^2$  that change systematically with time. Because of this nonsteady behavior in the morning and late afternoon, the analysis presented in subsequent sections will only focus on data collected between 1100 and 1700 LT.

The  $w$  skewness profile changes in both magnitude and shape through the morning until 1030 LT ([Fig. 4b](#)).

The peak value of the skewness increases from an altitude near  $0.35z_i$  early in the day to  $0.65z_i$  later in the day. For example, for the altitude of  $0.35z_i$ , the skewness is nearly constant after 1030 LT (Fig. 4e). The behavior is different at an altitude of  $0.75z_i$ , where the skewness is relatively small before 1330 LT and then increases and remains large until 1630 LT (Fig. 4e). This behavior is likely associated with large coherent thermals that occur in the afternoon, such as those seen in Fig. 1.

As compared with  $\sigma_w^2/w_*^2$  and skewness, the kurtosis does not change much over the course of the day (Fig. 4c) and is nearly always greater than 3 (the value for a Gaussian distribution). There is some decrease in kurtosis lower in the boundary layer and some increase higher in the boundary layer with time (Fig. 4f), with the largest difference between the two altitudes occurring near 1300 LT. This behavior indicates that there is a relative decrease in frequency of more extreme values of  $w$  at lower altitudes as the day progresses.

All of the median values of  $\sigma_w^2/w_*^2$  that were computed using the CDL data are smaller than the values reported by Lenschow et al. (2012), which are nearly the same magnitude as the 75th percentile of  $\sigma_w^2/w_*^2$  at 1530 LT for the SGP. The reason for this difference is not immediately clear, because it is anticipated that the CDL would underestimate the variance by only 9% on the basis of the laser pulse width and the range-gate size and because the values of  $u_*$ ,  $w_*$ , and stability are similar between the two studies. Note, however, that the study of Lenschow et al. (2012) is focused on a relatively small number of days and that our results are generally consistent with those of Hogan et al. (2009) as measured at the Chilbolton Observatory located in England.

*b. Variation with mean wind direction*

The area around the SGP is surrounded by a combination of pasture and cropland with relatively little topographic variability (Sisterson et al. 2016), and it is perhaps surprising that the profiles of  $\sigma_w^2/w_*^2$  sorted by wind direction (into bins that are  $22.5^\circ$  wide) show systematic variations (Fig. 5). In addition, the median value of  $\sigma_w^2/w_*^2$  for cases with southerly winds is systematically smaller than that measured during periods with easterly or westerly winds. The reason for this behavior is not obvious, although the sonic anemometer used in this analysis is located at the northern edge of a field near the SGP site, and its measurements are most representative for cases with southerly winds. There are also many more observations for cases with southerly winds; this could lead to some discrepancies with the measurements from other wind directions. Because of the observed sensitivity of the turbulence

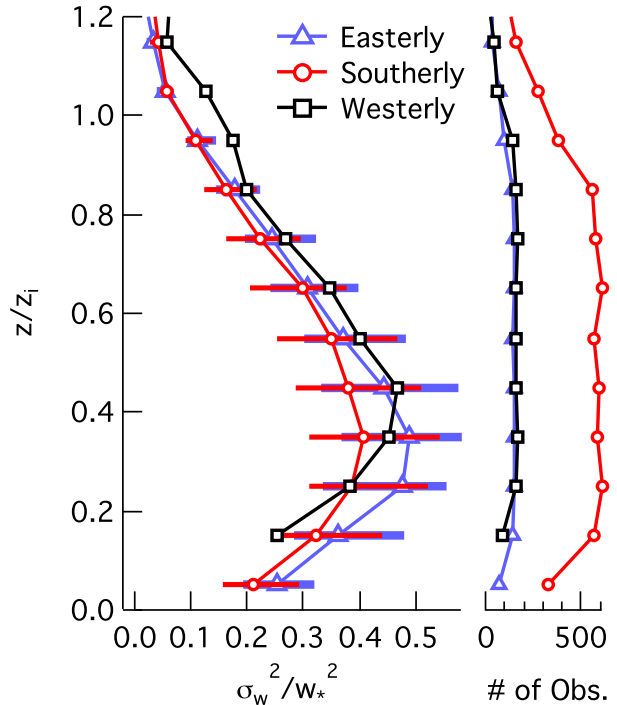


FIG. 5. Profiles of median  $\sigma_w^2/w_*^2$  for easterly (blue), southerly (red), and westerly (black) winds, with the corresponding total numbers of observations for each wind direction given to the right. Bars for easterly and southerly winds indicate the 75th and 25th percentiles.

statistics to the wind direction, the analysis associated with other meteorological variables will focus only on cases in which the mean wind direction measured by the CDL at  $0.5z_i$  is between  $135^\circ$  and  $225^\circ$ .

The results presented on the right-hand side of Fig. 5 highlight the rapid decrease in the number of good observations between normalized heights of  $0.8z_i$  and  $1.0z_i$ . This decrease is largely associated with the maximum range of the CDL and the relatively small amounts of aerosol loading near the boundary layer top. The median value of  $z_i$  between 1100 and 1700 LT is 1.40 km, and the 75th and 90th percentiles are 1.64 and 1.85 km, respectively. We see that there are many instances in which the unit will struggle to retrieve high-quality  $w$  statistics near the boundary layer top. This is one reason why RWP data are applied in section 4f to examine the impact of wind shear across the boundary layer top on the turbulence in the boundary layer.

*c. Variation with season*

One advantage of a long-term dataset is the ability to investigate the variability of important parameters across different seasons. In this case, we have divided the data into 3-month blocks, and values of  $\sigma_w^2/w_*^2$ ,

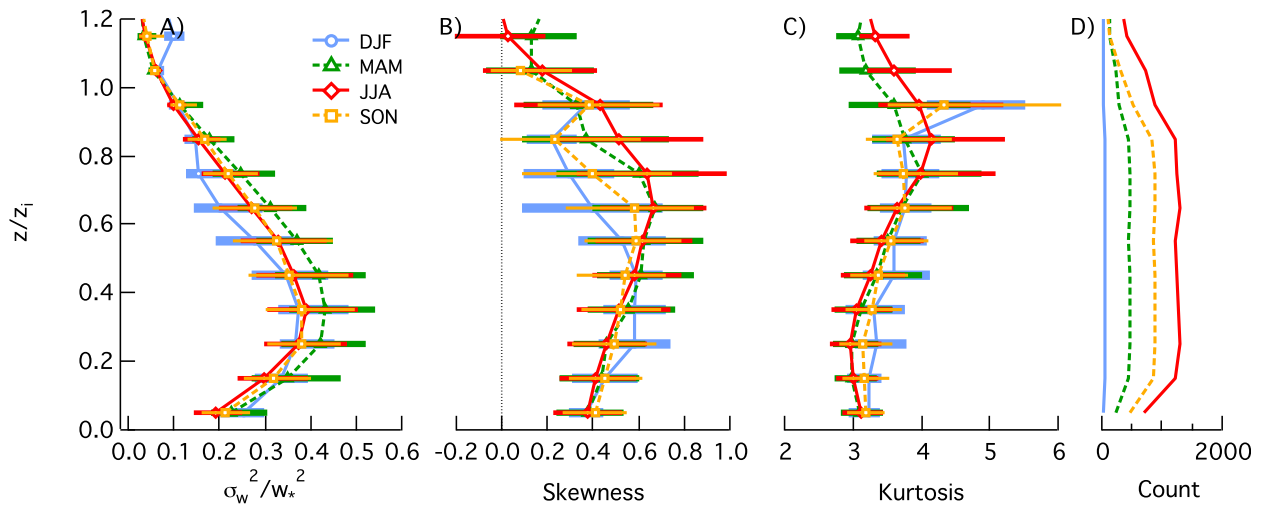


FIG. 6. Profiles of (a)  $\sigma_w^2/w_*^2$ , (b) skewness, (c) kurtosis, and (d) number of observations during the winter (blue), spring (green), summer (red), and fall (orange). For (a)–(c), the open symbols represent the median values and the bars indicate the 75th and 25th percentiles.

skewness, and kurtosis have been computed as a function of height (Fig. 6). The values of  $\sigma_w^2/w_*^2$  at all altitudes lower than  $0.8z_i$  are found to be largest in the spring, with moderate values found in the summer and autumn. The differences in  $\sigma_w^2/w_*^2$  are small between the winter and summer, although they are still statistically significant for altitudes between  $0.55z_i$  and  $0.75z_i$ . Overall, the skewness profiles for the warmer seasons are similar in shape to the profiles presented by LeMone (1990), with the largest values occurring near the middle of the boundary layer. There are seasonal differences in skewness above  $0.5z_i$ , with the wintertime values being smaller than those found in any other season. This behavior could be related to reduced surface heating and a reduced intensity of the convective thermals during winter. The kurtosis profiles have small seasonal differences until an altitude of  $0.8z_i$ , but there are only a

small number of observations at this height, and the differences may not be statistically significant.

#### d. Variation with $u_*$

The surface stress, as represented by  $u_*$ , is found to be related to the variability in the vertical profiles of  $w$  turbulence statistics. Values of  $u_*$  have been computed using data from the sonic anemometer deployed at the ARM SGP site, and the distribution of  $u_*$  is presented in Fig. 7. The data have been sorted into three difference classes according to the observed values of  $u_*$ : one for  $u_*$  of less than  $0.28 \text{ m s}^{-1}$ , one for values that are greater than  $0.59 \text{ m s}^{-1}$ , and one intermediate class. These values represent the 15th and 85th percentiles of the  $u_*$  distribution, and the range is roughly consistent with the thresholds applied in Lenschow et al. (2012), where  $u_*$  was found to range between  $0.16$  and  $0.52 \text{ m s}^{-1}$ .

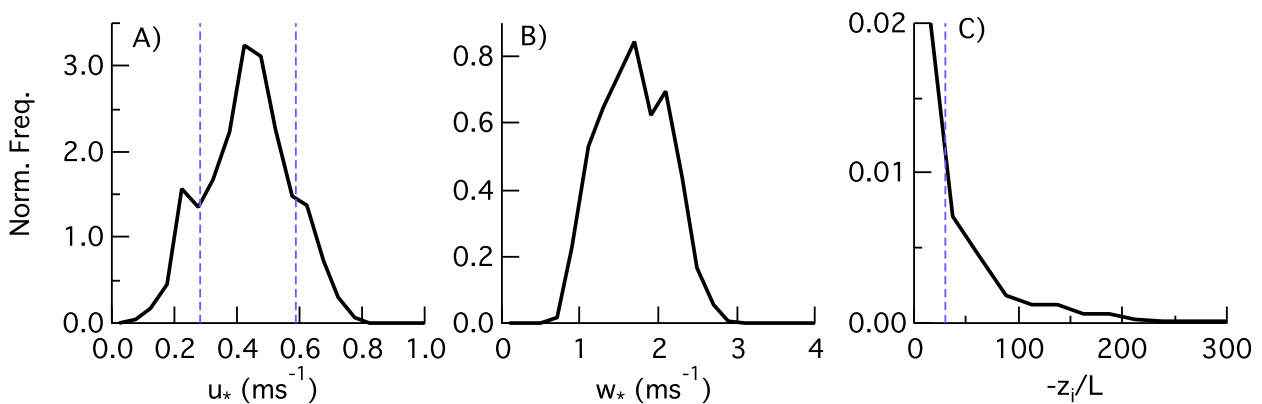


FIG. 7. Histograms of (a)  $u_*$ , (b)  $w_*$ , and (c)  $-z_i/L$  for periods used in the analysis of  $w$  statistics. The dashed lines in (a) and (c) indicate thresholds used for separating cases with small and large values.

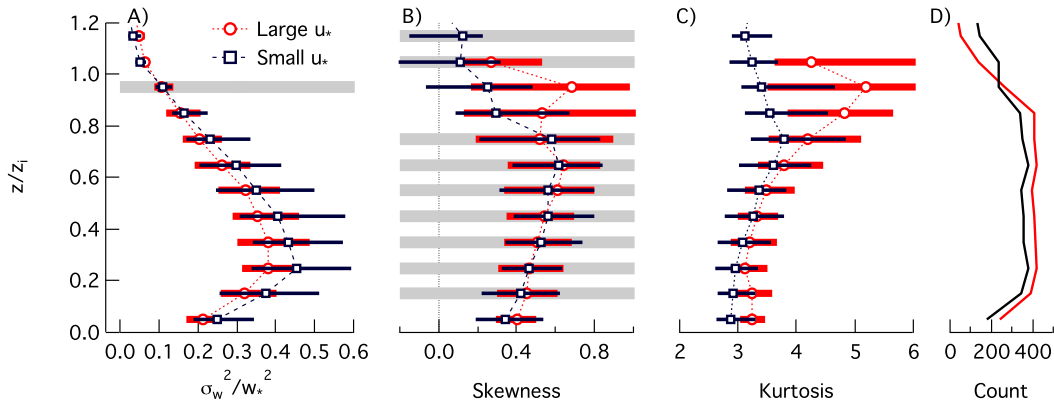


FIG. 8. Profiles of (a)  $\sigma_w^2/w_*^2$ , (b) skewness, (c) kurtosis, and (d) number of observations for cases with large (red) and small (black)  $u_*$ . For (a)–(c), the open symbols represent the median values and the bars indicate the 75th and 25th percentiles. Gray shading indicates heights at which the differences in the two distributions are not statistically significant at the 0.01 significance level.

Significant differences are found in the vertical profiles of  $\sigma_w^2/w_*^2$ , with smaller values of  $u_*$  corresponding to generally larger values of  $\sigma_w^2/w_*^2$  (Fig. 8a). The difference is particularly clear for altitudes of less than  $0.5z_i$ , with generally smaller differences in the upper part of the boundary layer. The skewness is not strongly affected by changes in  $u_*$ , at least for altitudes of lower than  $0.8z_i$  (Fig. 8b). It is interesting to note the changes in skewness aloft. Given the dependence of  $u_*$  on the surface measurements, this result is surprising. There is a weak tendency toward smaller values of wind shear across the boundary layer top for cases with large  $u_*$  (not shown) as well as an increase in wind shear at the boundary layer top during winter conditions. We will see in section 4f that the shape of the skewness profile is reminiscent of the plots for cases with small

and large wind shear at the boundary layer top. Large values of  $u_*$  are also associated with larger values of kurtosis (Fig. 8c), indicating an increase in extreme values associated with enhanced mixing for cases with large  $u_*$ .

*e. Variation with stability*

The static stability can be represented with the parameter  $-z_i/L$ , where  $L$  is the Obukhov length. In their study, Lenschow et al. (2012) used a threshold value of 30 to separate moderately unstable conditions and very unstable conditions. The same threshold is applied in this study. The median value of  $\sigma_w^2/w_*^2$  is found to be smaller in very unstable conditions in the bottom half of the boundary layer and to be slightly larger in the top half (Fig. 9a). These findings are

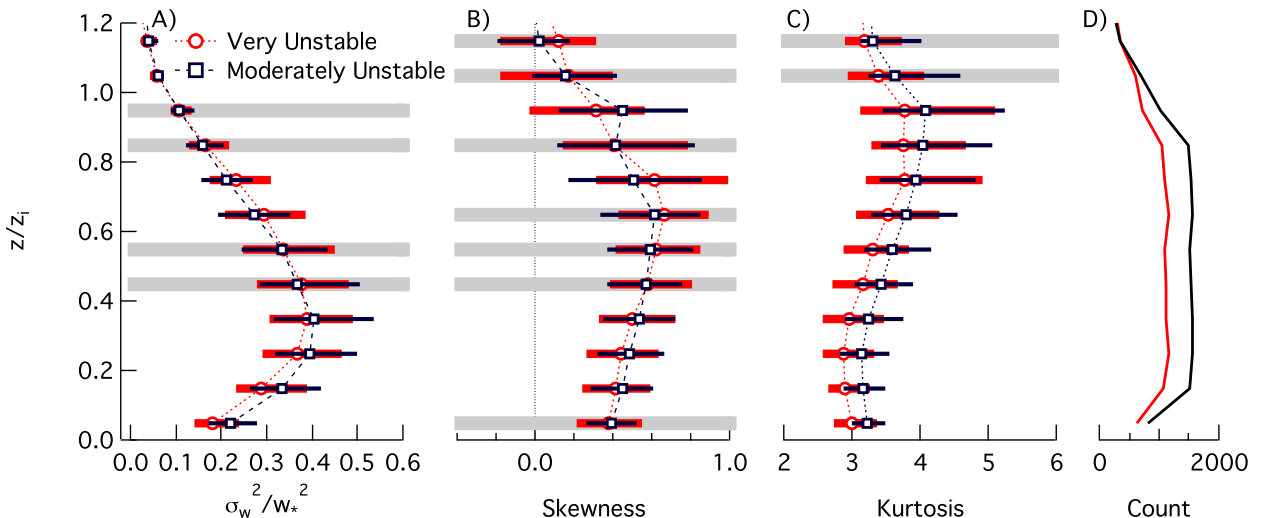


FIG. 9. As in Fig. 8, but for very unstable (red) and moderately unstable (black) conditions.

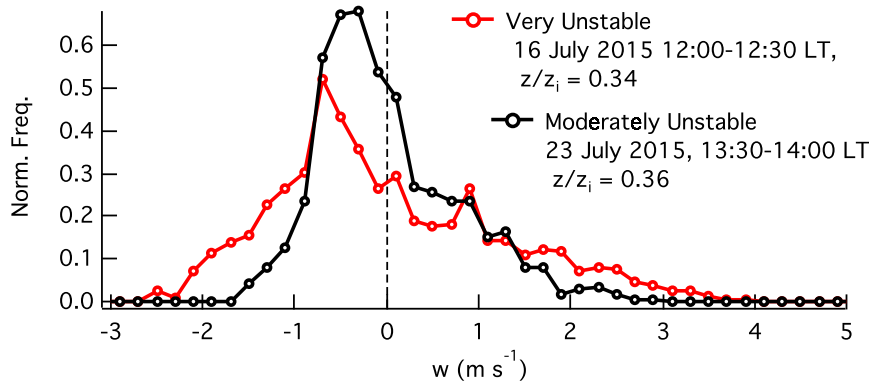


FIG. 10. PDFs of  $w$  for very unstable (red) and moderately unstable (black) conditions observed with the CDL.

consistent with those of Moeng and Sullivan (1994), who showed slightly larger values of normalized  $w$  variance during less-unstable conditions (albeit with a modified version of the scaling). This finding is different than that reported by Lenschow et al. (2012), who also found slightly larger values of  $\sigma_w^2/w_*^2$  during periods that are more unstable. It is important to note, however, that there is a large amount of variability in the values of  $\sigma_w^2/w_*^2$  computed from the CDL and that there are also cases (as shown in Fig. 10) in which the variance is larger for a more unstable case. This analysis also ignores the impact of wind shear on the PBL, which also has an impact on the nature of the turbulence. The differences in stability have minimal impact on skewness, although the small differences for altitudes below  $0.5z_i$  (with the exception of the lowest level) are found to be statistically significant (Fig. 9b). The kurtosis is found to be smaller in very unstable conditions (Fig. 9c), corresponding to a distribution that is less peaked and that tends to have fewer extreme values away from the mean value (Fig. 10). In some sense, this is consistent with the findings for  $u_*$ , for which increased values of  $u_*$  (which are likely associated with moderate instability) lead to increased values of kurtosis.

#### f. Variation with wind shear

The suite of instruments deployed at the SGP Central Facility provides a unique opportunity to examine changes in  $w$  turbulence statistics with changes in the wind shear across the boundary layer top. Rather than use the wind shear calculated from the CDL, we have used data from the RWP. As pointed out earlier, the number of good CDL observations drops off quickly near the boundary layer top. This drop-off makes the calculation of the wind shear across the boundary layer top difficult. The RWP retrieves wind profiles through the boundary layer on a more regular basis (although the

number of points used in the analysis is still relatively small) with a vertical resolution of 60 m. The wind shear is simply calculated as the difference in wind speed between  $0.9z_i$  and  $1.1z_i$ , and directional shear is ignored in this approach. Small and large values of shear are defined to be  $-0.6$  and  $1.4 \text{ m s}^{-1}$ , respectively. These values are approximately the 30th and 70th percentiles of the observed shear values derived from the RWP. The impact of the wind shear on the  $\sigma_w^2/w_*^2$  profile is evident for altitudes between  $0.4z_i$  and  $0.9z_i$  (Fig. 11a), with large amounts of shear leading to greater values of  $\sigma_w^2/w_*^2$ . There is also an impact on the skewness, with small amounts of wind shear being associated with distributions that are less skewed (Fig. 11b), although nearly all of these differences were not significant at the 0.01 level (the differences are significant at the 0.05 level for altitudes ranging from  $0.45z_i$  to  $0.95z_i$ , and the results are consistent with a similar analysis that is based on the CDL data). Larger amounts of wind shear also lead to an increase in kurtosis at the top of the boundary layer (Fig. 11c), indicating that the  $w$  distributions tend to have more values near the mean and additional outliers when the shear is large.

## 5. Summary and conclusions

This study helps to fill a void associated with a lack of long-term observations of the characteristics of turbulence over the depth of the cloud-free CBL. We utilized 1 yr of data collected using the CDL deployed at the ARM SGP site to document the characteristics of  $\sigma_w^2$ ,  $w$  skewness, and  $w$  kurtosis from the surface to the boundary layer top. The CDL data were sorted as a function of time of day, season,  $u_*$ , static stability, and wind shear across the top of the boundary layer to determine the impact of changes in these variables on the  $w$  statistics.

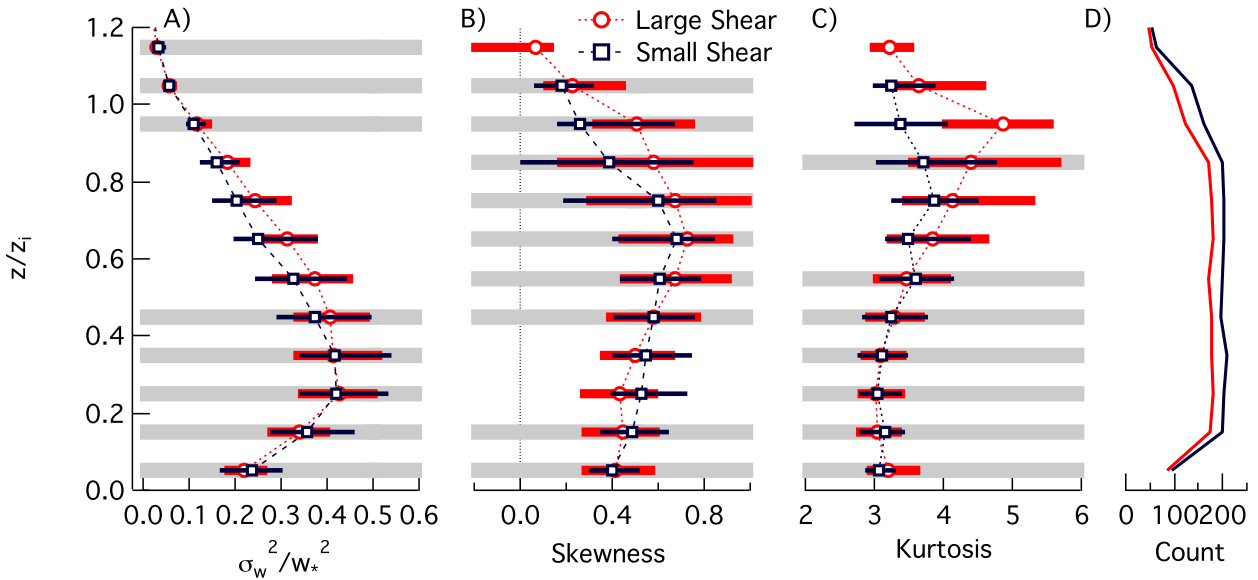


FIG. 11. As in Fig. 8, but for large (red) and small (black) amounts of wind shear across the boundary layer top.

Standard boundary layer scaling parameters were used to normalize the CDL observations; although profiles of  $\sigma_w^2/w_*^2$  collected during the afternoon collapsed onto a single curve, different results were found in the morning when the value of  $z_i$  changes rapidly. This breakdown in the standard scaling is likely due to non-stationarity in the morning boundary layer over the 30-min averaging intervals used here. Our results highlight that care is needed when applying traditional scaling during periods in which properties of the boundary layer are changing. The shape of the  $w$  skewness profiles also changed over the course of the day, whereas the  $w$  kurtosis profiles changed relatively little.

The  $w$  statistics were found to be sensitive to season,  $u_*$ , static stability within the boundary layer, and wind shear across the boundary layer top, although the details of the sensitivity changed depending on the variable of interest. The largest values of  $\sigma_w^2/w_*^2$  were found in the spring, with moderate values in the autumn and summer and smaller values in the winter. The  $w$  skewness profiles from the spring, summer, and autumn were very similar below  $0.5z_i$ , and the skewness above  $0.5z_i$  was smaller in the winter than in the other seasons. Larger values of  $u_*$  were found to lead to smaller values of  $\sigma_w^2/w_*^2$  and larger values of  $w$  kurtosis. Little difference was found in the  $w$  skewness for altitudes below  $0.7z_i$ , but large values of  $u_*$  were found to correspond to large values of skewness in the top half of the boundary layer. This behavior may be attributed to a reduction of wind shear across the boundary layer top during windy conditions. Very unstable conditions are generally associated with smaller amounts of  $\sigma_w^2/w_*^2$  in the bottom of the CBL, larger

amounts in the top of the layer, and smaller values of  $w$  kurtosis but little change in the  $w$  skewness. The magnitude of the wind shear across the boundary layer top has an impact on the  $\sigma_w^2/w_*^2$  in the top half of the boundary layer. In addition, large amounts of shear are associated with larger values of  $w$  kurtosis near the boundary layer top.

Long-term datasets, like the CDL data generated by the ARM Program, provide a unique opportunity to extend our understanding to include a wider range of meteorological conditions than has been possible in the past. In addition to insights gained about the vertical structure of turbulence in the boundary layer, studies such as this one can be used to evaluate parameterizations used in regional- and global-scale models. Future efforts will focus on combining data from the CDL with other instruments at the ARM sites to link the turbulence statistics with the thermodynamic properties and to examine bulk models of entrainment flux, such as those proposed by Sorbjan (1991, 2005), Conzemius and Fedorovich (2006), and Wulfmeyer et al. (2016).

*Acknowledgments.* This research was supported by the Office of Science of the U.S. Department of Energy as part of the Atmospheric Radiation Measurement (ARM) and Atmospheric System Research (ASR) programs, including partial support of authors Berg and Newsom via Grant KP1701000/57131 and author Turner via Grant DE-SC0014375. We thank Dr. Hailong Wang of Pacific Northwest National Laboratory for a careful review of the manuscript. The Pacific Northwest National Laboratory is operated for DOE by the Battelle Memorial Institute under Contract DE-A06-76RLO 1830. The data used in this paper

are available from the ARM data archive (<http://www.arm.gov>) or from the corresponding author.

## REFERENCES

- Banta, R. M., R. K. Newsom, J. K. Lundquist, Y. L. Pichugina, R. L. Coulter, and L. Mahrt, 2002: Nocturnal low-level jet characteristics over Kansas during CASES-99. *Bound.-Layer Meteor.*, **105**, 221–252, doi:10.1023/A:1019992330866.
- Berg, L. K., and R. B. Stull, 2005: A simple parameterization coupling the convective daytime boundary layer and fair-weather cumuli. *J. Atmos. Sci.*, **62**, 1976–1988, doi:10.1175/JAS3437.1.
- , and E. I. Kassianov, 2008: Temporal variability of fair-weather cumulus statistics at the ACRF SGP site. *J. Climate*, **21**, 3344–3358, doi:10.1175/2007JCLI2266.1.
- , —, C. N. Long, and D. L. Mills Jr., 2011: Surface summertime radiative forcing by shallow cumuli at the Atmospheric Radiation Measurement Southern Great Plains site. *J. Geophys. Res.*, **116**, D01202, doi:10.1029/2010JD014593.
- , W. I. Gustafson, E. I. Kassianov, and L. Deng, 2013: Evaluation of a modified scheme for shallow convection: Implementation of CuP and case studies. *Mon. Wea. Rev.*, **141**, 134–147, doi:10.1175/MWR-D-12-00136.1.
- Beyrich, F., 1997: Mixing height estimation from sodar data—A critical discussion. *Atmos. Environ.*, **31**, 3941–3953, doi:10.1016/S1352-2310(97)00231-8.
- Bianco, L., and J. M. Wilczak, 2002: Convective boundary layer depth: Improved measurement by Doppler radar wind profiler using fuzzy logic methods. *J. Atmos. Oceanic Technol.*, **19**, 1745–1758, doi:10.1175/1520-0426(2002)019<1745:CBLDIM>2.0.CO;2.
- Bretherton, C. S., and M. C. Wyant, 1997: Moisture transport, lower-tropospheric stability, and decoupling of cloud-topped boundary layers. *J. Atmos. Sci.*, **54**, 148–167, doi:10.1175/1520-0469(1997)054<0148:MTL TSA>2.0.CO;2.
- , J. R. McCaa, and H. Grenier, 2004: A new parameterization for shallow cumulus convection and its application to marine subtropical cloud-topped boundary layers. Part I: Description and 1D results. *Mon. Wea. Rev.*, **132**, 864–882, doi:10.1175/1520-0493(2004)132<0864:ANPFSC>2.0.CO;2.
- Brooks, I. M., 2003: Finding boundary layer top: Application of a wavelet covariance transform to lidar backscatter profiles. *J. Atmos. Oceanic Technol.*, **20**, 1092–1105, doi:10.1175/1520-0426(2003)020<1092:FBLTAO>2.0.CO;2.
- Browning, K. A., and R. Wexler, 1968: The determination of kinematic properties of a wind field using Doppler radar. *J. Appl. Meteor.*, **7**, 105–113, doi:10.1175/1520-0450(1968)007<0105:T DOKPO>2.0.CO;2.
- Clothiaux, E. E., T. P. Ackerman, G. G. Mace, K. P. Moran, R. T. Marchand, M. A. Miller, and B. E. Martner, 2000: Objective determination of cloud heights and radar reflectivities using a combination of active remote sensors at the ARM CART sites. *J. Appl. Meteor.*, **39**, 645–665, doi:10.1175/1520-0450(2000)039<0645:ODOCHA>2.0.CO;2.
- Conzemius, R. J., and E. Fedorovich, 2006: Dynamics of sheared convective boundary layer entrainment. Part II: Evaluation of bulk model predictions of entrainment flux. *J. Atmos. Sci.*, **63**, 1179–1199, doi:10.1175/JAS3696.1.
- Cook, D. R., 1997: Eddy correlation flux measurement system (30ECOR). Atmospheric Radiation Measurement Climate Research Facility Data Archive, accessed 2 February 2016, doi:10.5439/1025039.
- , 2016: Eddy correlation flux measurement system instrument handbook. ARM Tech. Rep. DOE/SC-ARM/TR-052, 18 pp. [Available online at [https://www.arm.gov/publications/tech\\_reports/handbooks/ecor\\_handbook.pdf](https://www.arm.gov/publications/tech_reports/handbooks/ecor_handbook.pdf).]
- Coulter, R., 2012: Radar wind profiler and RASS handbook. ARM Tech. Rep. DOE/SC-ARM-TR-044, 23 pp. [Available online at [https://www.arm.gov/publications/tech\\_reports/handbooks/rwp\\_handbook.pdf](https://www.arm.gov/publications/tech_reports/handbooks/rwp_handbook.pdf).]
- Darbieu, and Coauthors, 2015: Turbulence vertical structure of the boundary layer during the afternoon transition. *Atmos. Chem. Phys.*, **15**, 10 071–10 086, doi:10.5194/acp-15-10071-2015.
- Davis, J., C. Collier, F. Davies, R. Burton, G. Pearson, and P. Di Girolamo, 2013: Vertical velocity observed by Doppler lidar during COPS-A case study with convective rain event. *Meteor. Z.*, **22**, 463–470, doi:10.1127/0941-2948/2013/0411.
- Deardorff, J. W., 1974: Three-dimensional numerical study of turbulence in an entraining mixed layer. *Bound.-Layer Meteor.*, **7**, 199–226, doi:10.1007/BF00227913.
- , and G. E. Willis, 1985: Further results from a laboratory model of the convective planetary boundary layer. *Bound.-Layer Meteor.*, **32**, 205–236, doi:10.1007/BF00121880.
- Dong, X., P. Minnis, and B. Xi, 2005: A climatology of mid-latitude continental clouds from the ARM SGP Central Facility: Part I: Low-level cloud macrophysical, microphysical, and radiative properties. *J. Climate*, **18**, 1391–1410, doi:10.1175/JCLI3342.1.
- Fang, M., B. A. Albrecht, V. P. Ghate, and P. Kollias, 2014: Turbulence in continental stratocumulus, part I: External forcings and turbulence structures. *Bound.-Layer Meteor.*, **150**, 341–360, doi:10.1007/s10546-013-9873-3.
- Ghate, V. P., B. A. Albrecht, M. A. Miller, A. Brewer, and C. W. Fairall, 2014: Turbulence and radiation in stratocumulus-topped marine boundary layers: A case study from VOCALS-REx. *J. Appl. Meteor. Climatol.*, **53**, 117–135, doi:10.1175/JAMC-D-12-0225.1.
- Greenhut, G. K., and S. J. S. Khalsa, 1987: Convective elements in the marine atmospheric boundary layer. Part I: Conditional sampling statistics. *J. Climate Appl. Meteor.*, **26**, 813–822, doi:10.1175/1520-0450(1987)026<0813:CEITMA>2.0.CO;2.
- Heffter, J. L., 1980: Air Resources Laboratories atmospheric transport and dispersion model. ARL Tech. Memo. ERL ARL-81, 24 pp. [Available online at <https://www.arl.noaa.gov/documents/reports/arl-81.pdf>.]
- Hogan, R. J., A. L. M. Grant, A. J. Illingworth, G. N. Pearson, and E. J. O'Connor, 2009: Vertical velocity variance and skewness in clear and cloud-topped boundary layers as revealed by Doppler lidar. *Quart. J. Roy. Meteor. Soc.*, **135**, 635–643, doi:10.1002/qj.413.
- Holdridge, D., and J. Kyrouac, 1993: Surface meteorological instrumentation (MET). Atmospheric Radiation Measurement Climate Research Facility Data Archive, accessed 2 February 2016, doi:10.5439/1025220.
- Holzworth, G. C., 1964: Estimates of mean maximum mixing depths in the contiguous United States. *Mon. Wea. Rev.*, **92**, 235–242, doi:10.1175/1520-0493(1964)092<0235:EOMMMD>2.3.CO;2.
- , 1967: Mixing depths, wind speeds and air pollution potential for selected locations in the United States. *J. Appl. Meteor.*, **6**, 1039–1044, doi:10.1175/1520-0450(1967)006<1039:MDWSAA>2.0.CO;2.
- Iwai, H., S. Ishii, R. Oda, K. Mizutani, S. Sekizawa, and Y. Murayama, 2013: Performance and technique of coherent 2- $\mu$ m differential absorption and wind lidar for wind measurement.

- J. Atmos. Oceanic Technol.*, **30**, 429–449, doi:10.1175/JTECH-D-12-00111.1.
- Kain, J. S., 2004: The Kain–Fritsch convective parameterization: An update. *J. Appl. Meteor.*, **43**, 170–181, doi:10.1175/1520-0450(2004)043<0170:TKCPAU>2.0.CO;2.
- , and J. M. Fritsch, 1990: A one-dimensional entraining/detraining plume model and its application in convective parameterization. *J. Atmos. Sci.*, **47**, 2784–2802, doi:10.1175/1520-0469(1990)047<2784:AODEPM>2.0.CO;2.
- Larson, V. E., D. P. Schanen, M. H. Wang, M. Ovchinnikov, and S. Ghan, 2012: PDF parameterization of boundary layer clouds in models with horizontal grid spacings from 2 to 16 km. *Mon. Wea. Rev.*, **140**, 285–306, doi:10.1175/MWR-D-10-05059.1.
- LeMone, M. A., 1990: Some observations of vertical velocity skewness in the convective planetary boundary layer. *J. Atmos. Sci.*, **47**, 1163–1169, doi:10.1175/1520-0469(1990)047<1163:SOOVVS>2.0.CO;2.
- Lenschow, D. H., and P. L. Stephens, 1980: The role of thermals in the convective boundary layer. *Bound.-Layer Meteor.*, **19**, 509–532, doi:10.1007/BF00122351.
- , and J. Sun, 2007: The spectral composition of fluxes and variances over land and sea out to the mesoscale. *Bound.-Layer Meteor.*, **125**, 63–84, doi:10.1007/s10546-007-9191-8.
- , J. C. Wyngaard, and W. T. Pennell, 1980: Mean-field and second-moment budgets in a baroclinic, convective boundary layer. *J. Atmos. Sci.*, **37**, 1313–1326, doi:10.1175/1520-0469(1980)037<1313:MFASMB>2.0.CO;2.
- , V. Wulfmeyer, and C. Senff, 2000: Measuring second-through fourth-order moments in noisy data. *J. Atmos. Oceanic Technol.*, **17**, 1330–1347, doi:10.1175/1520-0426(2000)017<1330:MSTFOM>2.0.CO;2.
- , M. Lothon, S. Mayor, P. Sullivan, and G. Canut, 2012: A comparison of higher-order vertical velocity moments in the convective boundary layer from lidar with in situ measurements and large-eddy simulation. *Bound.-Layer Meteor.*, **143**, 107–123, doi:10.1007/s10546-011-9615-3.
- Liu, L., F. Hu, and X.-L. Cheng, 2011: Probability density functions of turbulent velocity and temperature fluctuations in the unstable atmospheric surface layer. *J. Geophys. Res.*, **116**, D12117, doi:10.1029/2010JD015503.
- Liu, S., and X.-Z. Liang, 2010: Observed diurnal cycle climatology of planetary boundary layer height. *J. Climate*, **23**, 5790–5809, doi:10.1175/2010JCLI3552.1.
- Lundquist, J. K., and Coauthors, 2017: Assessing state-of-the-art capabilities for probing the atmospheric boundary layer: The XPIA field campaign. *Bull. Amer. Meteor. Soc.*, **98**, 289–314, doi:10.1175/BAMS-D-15-00151.1.
- Martin, S., F. Beyrich, and J. Bange, 2014: Observing entrainment processes using a small unmanned aerial vehicle: A feasibility study. *Bound.-Layer Meteor.*, **150**, 449–467, doi:10.1007/s10546-013-9880-4.
- Mather, J. H., and J. W. Voyles, 2012: The ARM Climate Research Facility: A review of structure and capabilities. *Bull. Amer. Meteor. Soc.*, **94**, 377–392, doi:10.1175/BAMS-D-11-00218.1.
- Maurer, V., N. Kalthoff, A. Wieser, M. Kohler, M. Mauder, and L. Gantner, 2016: Observed spatiotemporal variability of boundary-layer turbulence over flat, heterogeneous terrain. *Atmos. Chem. Phys.*, **16**, 1377–1400, doi:10.5194/acp-16-1377-2016.
- Moeng, C.-H., and P. P. Sullivan, 1994: A comparison of shear- and buoyancy-driven planetary boundary layer flows. *J. Atmos. Sci.*, **51**, 999–1022, doi:10.1175/1520-0469(1994)051<0999:ACOSAB>2.0.CO;2.
- Muradyan, P., T. Martin, and R. Coulter, 1998: Radar wind profiler (915RWPWINDCON). Atmospheric Radiation Measurement Climate Research Facility, accessed 7 March 2016, doi:10.5439/1025135.
- Newsom, R. K., 2012: Doppler lidar handbook. ARM Tech. Rep. DOE/SC-ARM-TR-101, 16 pp. [Available online at [https://www.arm.gov/publications/tech\\_reports/handbooks/dl\\_handbook.pdf](https://www.arm.gov/publications/tech_reports/handbooks/dl_handbook.pdf).]
- , C. Sivaraman, T. R. Shippert, and L. D. Riihimaki, 2015: Doppler lidar vertical velocity statistics value-added product. ARM Tech. Rep. DOE/SC-ARM/TR-149, 12 pp. [Available online at [https://www.arm.gov/publications/tech\\_reports/doe-sc-arm-tr-149.pdf](https://www.arm.gov/publications/tech_reports/doe-sc-arm-tr-149.pdf).]
- , W. A. Brewer, J. M. Wilczak, D. E. Wolfe, S. P. Oncley, and J. K. Lundquist, 2017: Validating precision estimates in horizontal wind measurements from a Doppler lidar. *Atmos. Meas. Tech.*, **10**, 1229–1240, doi:10.5194/amt-10-1229-2017; Corrigendum, doi:10.5194/amt-10-1229-2017-corrigendum.
- Pearson, G., F. Davies, and C. Collier, 2009: An analysis of the performance of the UFAM pulsed Doppler lidar for observing the boundary layer. *J. Atmos. Oceanic Technol.*, **26**, 240–250, doi:10.1175/2008JTECHA1128.1.
- Röhner, L., and K. Träumner, 2013: Aspects of convective boundary layer turbulence measured by a dual-Doppler lidar system. *J. Atmos. Oceanic Technol.*, **30**, 2132–2142, doi:10.1175/JTECH-D-12-00193.1.
- Scarino, A. J., and Coauthors, 2014: Comparison of mixed layer heights from airborne high spectral resolution lidar, ground-based measurements, and the WRF-Chem model during CalNex and CARES. *Atmos. Chem. Phys.*, **14**, 5547–5560, doi:10.5194/acp-14-5547-2014.
- Seibert, P., F. Beyrich, S.-E. Gryning, S. Joffre, A. Rasmussen, and P. Tercier, 2000: Review and intercomparison of operational methods for the determination of the mixing height. *Atmos. Environ.*, **34**, 1001–1027, doi:10.1016/S1352-2310(99)00349-0.
- Sisterson, D. L., R. A. Pepler, T. S. Cress, P. J. Lamb, and D. D. Turner, 2016: The ARM Southern Great Plains (SGP) site. *The Atmospheric Radiation Measurement (ARM) Program: The First 20 Years, Meteor. Monogr.*, No. 57, Amer. Meteor. Soc., 6.1–6.14, doi:10.1175/AMSMONOGRAPHS-D-16-0004.1.
- Smedman, A.-S., and U. Högström, 1983: Turbulent characteristics of a shallow convective internal boundary layer. *Bound.-Layer Meteor.*, **25**, 271–287, doi:10.1007/BF00119540.
- Sorbjan, Z., 1991: Evaluation of local similarity functions in the convective boundary layer. *J. Appl. Meteor.*, **30**, 1565–1583, doi:10.1175/1520-0450(1991)030<1565:EOLSFI>2.0.CO;2.
- , 2005: Statistics of scalar fields in the atmospheric boundary layer based on large-eddy simulations. Part 1: Free convection. *Bound.-Layer Meteor.*, **116**, 467–486, doi:10.1007/s10546-005-0907-3.
- Stull, R. B., 1988: *An Introduction to Boundary Layer Meteorology*. Kluwer Academic, 666 pp.
- Troen, I. B., and L. Mahrt, 1986: A simple model of the atmospheric boundary layer; sensitivity to surface evaporation. *Bound.-Layer Meteor.*, **37**, 129–148, doi:10.1007/BF00122760.
- Tucker, S. C., C. J. Senff, A. M. Weickmann, W. A. Brewer, R. M. Banta, S. P. Sandberg, D. C. Law, and R. M. Hardesty, 2009: Doppler lidar estimation of mixing height using turbulence, shear, and aerosol profiles. *J. Atmos. Oceanic Technol.*, **26**, 673–688, doi:10.1175/2008JTECHA1157.1.

- Turner, D. D., V. Wulfmeyer, L. K. Berg, and J. H. Schween, 2014: Water vapor turbulence profiles in stationary continental convective mixed layers. *J. Geophys. Res. Atmos.*, **119**, 11 151–11 165, doi:[10.1002/2014JD022202](https://doi.org/10.1002/2014JD022202).
- Vogelmann, and Coauthors, 2012: RACORO extended-term aircraft observations of boundary layer clouds. *Bull. Amer. Meteor. Soc.*, **93**, 861–878, doi:[10.1175/BAMS-D-11-00189.1](https://doi.org/10.1175/BAMS-D-11-00189.1).
- White, A. B., C. J. Senff, and R. M. Banta, 1999: A comparison of mixing depths observed by ground-based wind profilers and an airborne lidar. *J. Atmos. Oceanic Technol.*, **16**, 584–590, doi:[10.1175/1520-0426\(1999\)016<0584:ACOMDO>2.0.CO;2](https://doi.org/10.1175/1520-0426(1999)016<0584:ACOMDO>2.0.CO;2).
- Williams, A. G., and J. M. Hacker, 1992: The composite shape and structure of coherent eddies in the convective boundary layer. *Bound.-Layer Meteor.*, **61**, 213–245, doi:[10.1007/BF02042933](https://doi.org/10.1007/BF02042933).
- Wood, C. R., and Coauthors, 2010: Turbulent flow at 190 m height above London during 2006–2008: A climatology and the applicability of similarity theory. *Bound.-Layer Meteor.*, **137**, 77–96, doi:[10.1007/s10546-010-9516-x](https://doi.org/10.1007/s10546-010-9516-x).
- Wulfmeyer, V., S. K. Muppa, A. Behrendt, E. Hammann, F. Späth, Z. Sorbjan, D. D. Turner, and R. M. Hardesty, 2016: Determination of convective boundary layer entrainment fluxes, dissipation rates, and the molecular destruction of variances: Theoretical description and a strategy for its confirmation with a novel lidar system synergy. *J. Atmos. Sci.*, **73**, 667–692, doi:[10.1175/JAS-D-14-0392.1](https://doi.org/10.1175/JAS-D-14-0392.1).
- Wyngaard, J. C., O. R. Coté, and Y. Izumi, 1971: Local free convection, similarity, and the budgets of shear stress and heat flux. *J. Atmos. Sci.*, **28**, 1171–1182, doi:[10.1175/1520-0469\(1971\)028<1171:LFCSAT>2.0.CO;2](https://doi.org/10.1175/1520-0469(1971)028<1171:LFCSAT>2.0.CO;2).
- Zhang, Y., and S. A. Klein, 2010: Mechanisms affecting the transition from shallow to deep convection over land: Inferences from observations of the diurnal cycle collected at the ARM Southern Great Plains site. *J. Atmos. Sci.*, **67**, 2943–2959, doi:[10.1175/2010JAS3366.1](https://doi.org/10.1175/2010JAS3366.1).